ACS OMEGA

Open Access



http://pubs.acs.org/journal/acsodf

Article

# $TiO_2$ Phase Ratio's Contribution to the Photocatalytic Activity

Anna Stepanova, Teddy Tite, Iryna Ivanenko, Monica Enculescu, Cristian Radu, Daniela Cristina Culita, Arpad Mihai Rostas,* and Aurelian Catalin Galca*

Cite This: *ACS Omega* 2023, 8, 41664−41673

Read Online

ACCESS | Metrics & More | Article Recommendations | Supporting Information

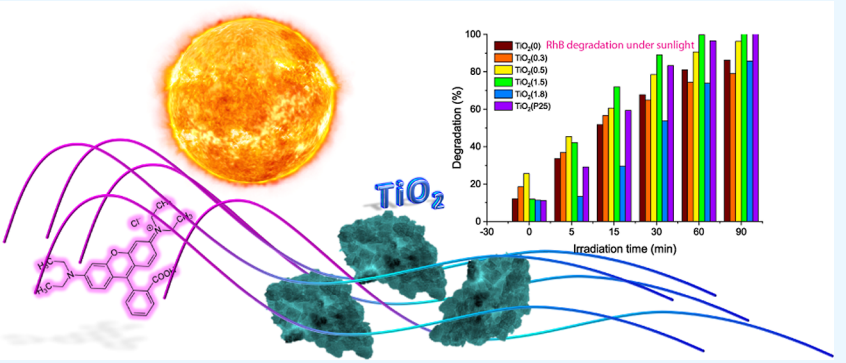


**ABSTRACT:** Photocatalysis is one of the approaches for solving environmental issues derived from extremely harmful pollution caused by industrial dyes, medicine, and heavy metals. Titanium dioxide is among the most promising photocatalytic semiconductors; thus, in this work, $TiO_2$ powders were prepared by a hydrothermal synthesis using titanium tetrachloride $TiCl_4$ as a Ti source. The effect of the hydrochloric acid (HCl) concentration on $TiO_2$ formation was analyzed, in which a thorough morpho-structural analysis was performed employing different analysis methods like XRD, Raman spectroscopy, SEM/TEM, and $N_2$ physisorption. EPR spectroscopy was employed to characterize the paramagnetic defect centers and the photogeneration of reactive oxygen species. Photocatalytic properties were tested by photocatalytic degradation of the rhodamine B (RhB) dye under UV light irradiation and using a solar simulator. The pH value directly influenced the formation of the $TiO_2$ phases; for less acidic conditions, the anatase phase of $TiO_2$ crystallized, with a crystallite size of ≈9 nm. Promising results were observed for $TiO_2$, which contained 76% rutile, showing a 96% degradation of RhB under the solar simulator and 91% under UV light after 90 min irradiation, and the best result showed that the sample with 67% of the anatase phase after 60 min irradiation under the solar simulator had a 99% degradation efficiency.

## 1. INTRODUCTION

The presence of harmful pollutants in water, including dyes, heavy metals, and drugs, is one of the main concerns nowadays. There are some effective methods to address the identified problem. For instance, there are several pollutant removal techniques, like adsorption,[1,2] coagulation,[3,4] membrane separation,[5] and reverse osmosis.[6] Dyes such as thymol blue, carmine, indigo red, red 120, rhodamine B, methylene blue, and eriochrome black-T are most often used in the textile industry.[7] When they get into wastewater, they become dangerous and cause serious harm to aquatic flora, fauna, and humans.[7,8] Photocatalysis is a well-known method, and its history began at the beginning of the 20th century.[9−12] However, it reasonably still attracts a lot of attention as an advanced oxidation process used for the photodegradation of toxic compounds and dyes.[13−18] To ensure a photocatalytic process, two conditions must be met, using light as an electron exciter and a semiconductor as a process catalyst. Simultaneously, photocatalysts must have electronic structure, charge transport characteristics, and light-absorbing properties.

Titanium dioxide ($TiO_2$) is the most widely used photocatalyst material.[19−21] The advantages of $TiO_2$ include nontoxicity, easy activation by ultraviolet light, chemical stability, environmental friendliness, the strong oxidizing ability of photogenerated holes, and chemical inertness,[9,19,22−24] making this material excellent in the decomposition of inorganic and organic pollutants.

During these years of research on synthesizing titanium oxide nanoparticles, the sol−gel,[25−27] hydrothermal method,[28−32] and chemical vapor[33] and liquid phase deposition[34,35]

Received: August 10, 2023
Revised: October 6, 2023
Accepted: October 10, 2023
Published: October 25, 2023

were most often used.[36,37] However, the sol−gel and hydrothermal methods have been identified as the most common and are simple to implement. The hydrothermal method is a relatively inexpensive method that ensures high purity and size uniformity of the synthesized one-dimensional $TiO_2$ nanostructures.[38−40] The process of crystallization of the substance occurs inside a Teflon or polypropylene autoclave and a stainless-steel vessel, which is stored at a temperature above 100 °C and a pressure of more than 1 atm. Compared with some synthesis methods (e.g., sol−gel), the hydrothermal approaches can significantly reduce the synthesis time. Although various studies have been carried out using hydrothermal approaches, only a few studies have investigated the influence of structural properties on the photodegradation process. Tang et al.[28] studied the effects of hydrothermal time on the structure and photocatalytic properties of $TiO_2$. According to their work, increasing the hydrothermal synthesis time was accompanied by the formation of a rutile phase. Obtaining the anatase phase is the aim of most researchers due to better photocatalytic activity, although the brookite phase might be the best.[41] Luttrell et al.[42] compared the activity of epitaxial rutile and anatase $TiO_2$ films in the photocatalytic decomposition of methyl orange. Their research confirmed the general notion of greater activity of anatase, with a film thickness of 20 nm, and with the same preparation conditions for both samples, the anatase (001) film showed twice the activity for the photocatalytic decomposition of organic molecules than the rutile (101) film. However, looking at the work of Li et al.,[43] which focused on the activity of materials with a mixed phase of $TiO_2$, the pure anatase did not show good comparable results. The mixed-phase samples showed higher photocatalytic activity, and the optimal ratio with the degree of degradation of rhodamine B around 75% is found to be 77% anatase and 23% rutile due to electron−hole separation, which is more efficient resulting from the combination of anatase and rutile.

Research by Khizir and Abbas[32] was focused on determining the optimal hydrothermal growth temperature in the diapason from 110 to 170 °C for the reaction time of 6 h for each sample deposition. As a result, it was noticed that increasing the growth temperature led to a decrease in the diameter of the nanorods. Moreover, in Tang's research, $TiO_2$ prepared at 180 °C displayed the best photocatalytic performance.[28]

Qi et al.[29] synthesized $TiO_2$ nanorod arrays using the hydrothermal method and HCl−$TiCl_4$ solution. However, they formed a $TiO_2$ layer on the surface of an indium−tin-oxide-coated glass (ITO). The authors noticed that when the reaction temperature increased from 140 to 180 °C, in $TiO_2$, the long side and length of the nanorods just increased, but no new crystalline phase was formed. When the temperature was lower than 160 °C, the quadrate side length and the length of nanorods were unchanged. Simultaneously, the arrangement of $TiO_2$ nanorods became more and more uniform when the temperature increased. The nanorods were transformed from a neat array to shrubbery by increasing the temperature to 180 °C. The study determined that the best results were achieved using 6 M hydrochloric acid, a quantity chosen as a reference for the current work.[29]

Many studies have used $TiO_2$ combined with other materials to boost its photocatalytic activity. For example, Li et al.[44] used $Ti_3C_2$ MXene as a cocatalyst for methyl orange degradation, reaching a degradation efficiency of 99.6% within 40 min. Zhu et al.[45] used a $Ag_3PO_4/TiO_2$ heterojunction for efficient photodegradation of rhodamine B with 100% efficiency. Li et al.[46] reported a comprehensive review of fluorinated $TiO_2$ for photocatalytic applications underlining the versatility of $TiO_2$-based photocatalysts.

In the present study, at a hydrothermal temperature of 160 °C and a short hydrothermal time of 6 h, $TiO_2$-based photocatalysts were prepared with different concentrations of HCl. Various methods and options exist to influence the synthesis of titanium dioxide under hydrothermal conditions. Zhao et al.[47] obtained different phases of $TiO_2$ depending on the HCl concentration, where the anatase phase was generated with a 1 M HCl concentration, whereas using a 0.05 M HCl no rutile was identified. The obtained samples were comprehensively characterized by X-ray diffraction, Raman spectroscopy, scanning/transmission electron microscopy, $N_2$ physisorption, and electron paramagnetic resonance spectroscopy, while the degradation of rhodamine B was monitored by employing UV−vis spectroscopy.

## 2. RESULTS AND DISCUSSION

**2.1. Morpho-structural and Optical Properties of the $TiO_2$ Samples.** Figure 1 shows the XRD patterns of the

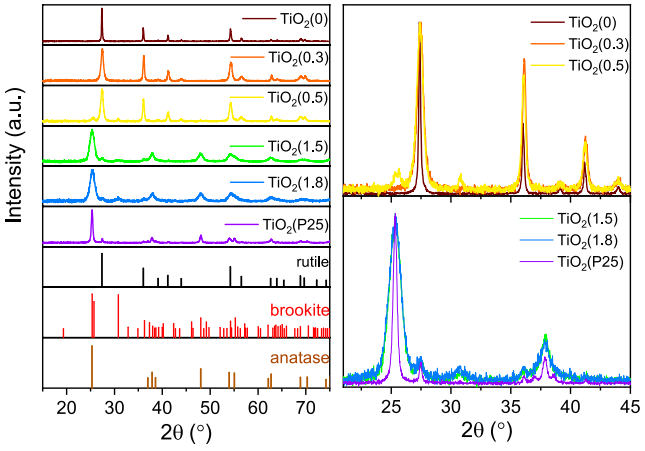


**Figure 1.** XRD patterns of the $TiO_2$ samples together with the diffraction peak positions of anatase, brookite, and rutile.

nanoparticles. For the samples $TiO_2(0)$ and $TiO_2(0.3)$, the intense diffraction peaks correspond to the 110, 101, 111, 210, 211, 220, 002, 310, 301, and 112 reflections of the rutile $TiO_2$ phase according to the ICDD file no. 01-086-4329, which was also confirmed by the selected area electron diffraction (SAED) measurements presented in Figures S1 and S2 in the Supporting Information. For $TiO_2(0.5)$, the main phase was determined as rutile but with some amount of anatase and brookite (ICDD file no. 04-007-0758), as confirmed by SAED patterns Figures S3 and S4. Regarding the samples $TiO_2(1.5)$ and $TiO_2(1.8)$, the XRD patterns matched with the strong diffraction peaks of anatase, which correspond to the 101, 004, 200, 205, and 204 reflections as indexed in the ICDD file no. 04-011-0664, and the low intense 110 reflection of rutile as well as the visible 211 diffraction line of brookite. SAED confirms these findings, the results being presented in Figures S5 and S6. Note that most of the brookite diffraction lines are overlapped by those of anatase,[48,49] and only the 211 reflection at $2\theta = 30.8°$ emphasizes the presence of the brookite phase. The average crystallite sizes of the studied $TiO_2$ were inferred from the XRD patterns using Scherer's formula.[50−53] The rutile


https://doi.org/10.1021/acsomega.3c05890
ACS Omega 2023, 8, 41664−41673

110, anatase 101, and the brookite 211 reflections were fitted using a Lorentz profile (see Figure S9 and Table T1), the fwhm used to calculate the coherence length along the corresponding crystallographic direction being the difference between the experimental fwhm and the instrument function.[54]

The size value decreased from an average of 64 to 9 nm due to the formation of anatase and brookite phases. During the analysis of the diffractograms, it was determined that some of the samples have a mixed-phase composition of $TiO_2$. The content of rutile in the sample can be calculated with eq 1:[55]

$$ {}^2W_R = \left(1 + \frac{I_R^{110}}{I_C} \cdot \frac{I_C}{I_A^{101}} \cdot \frac{A_A^{101}}{A_R^{110}}\right)^{-1} \quad (1) $$

where $I/I_c$ is the internal standard calibration constant from the powder diffraction file of the $TiO_2$ phase; $A_A$ and $A_R$ correspond to the integrated XRD intensities of the anatase 101 and rutile 110 diffraction lines. A brief description of the structural parameters and phase composition is given in Table 1.

**Table 1. Structural and Optical Properties of the $TiO_2$-Based Samples**[a]

| $TiO_2$ sample | $HCl/TiCl_4$ (molar) | R:A:B ($W_t$, %) | $D_m$ (nm) R | A | B | SSA ($m^2$ $g^{-1}$) | $E_g$ (eV) |
|---|---|---|---|---|---|---|---|
| (0) | 6:0.1 | 100:0:0 | 64 | | | 13.4 | 2.2 |
| (0.3) | 3:0.1 | 100:0:0 | 18 | | | 31.8 | 2.4 |
| (0.5) | 3:0.2 | 76:6:18 | 14 | 43 | 22 | 40.7 | 2.9 |
| (1.5) | 0.1:0.1 | 14:67:19 | 8 | 10 | 6 | 186.1 | 3.1 |
| (1.8) | 0:0.1 | 12:64:24 | 8 | 9 | 6 | 181.6 | 3.2 |
| (P25) | commercial | 12:88:0 | 37 | 25 | | 58.3 | 3.3 |

[a]Legend: R—rutile, A—anatase, and B—brookite $TiO_2$ phases, $D_m$—main diameter, SSA—specific surface area, and $E_g$—band gap.

In addition, the calculation of the ratio of the weight fraction of each phase in the sample with three phases, such as for $TiO_2$(0.5), $TiO_2$(1.5), and $TiO_2$(1.8), was performed using eq 2:[55]

$$ {}^2W_R = \left(\frac{I_R}{RIR_R \cdot I^{rel}} \cdot \left[\sum_{n=1}^{3} \frac{I_n}{RIR \cdot I^{rel}}\right]^{-1}\right) \quad (2) $$

where $RIR = I/I_c$; $n$—the number of phases in the mixture, $n = 3$; $I^{rel}$—relative intensity constant; $I^{rel} = 100$.

Raman spectroscopy is useful for determining the $TiO_2$ phases. It is complementary to XRD in analyzing the crystal structure of a material. Raman spectra of the synthesized samples, presented in Figure 2, show peaks corresponding to the main phases of $TiO_2$. The peaks at 237, 443, and 610 $cm^{-1}$ correspond to the rutile phase, those at 145, 197, 395, 515, and 638 $cm^{-1}$ correspond to the anatase phase,[22] while the peaks at 246 and 324 $cm^{-1}$ correspond to the brookite phase,[56] confirming the phase composition presented in Table 1 determined employing XRD.

The SEM image of the $TiO_2$(0) sample shows agglomerates of nanorods. The particles in the $TiO_2$(0.3) and $TiO_2$(0.5) samples have a spherical shape of agglomerates consisting of nanowires, as for samples $TiO_2$(1.5) and $TiO_2$(1.8), they do not have a clearly expressed shape and are extremely small to determine their morphological structure.

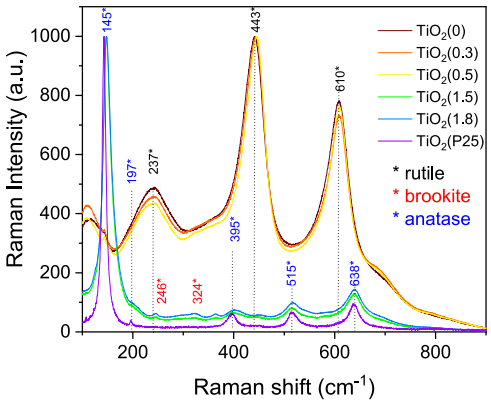


**Figure 2.** Raman spectra of the $TiO_2$ samples.

The transmission electron microscopy (TEM) images presented in Figures 3 and S1–S7 show that the sample $TiO_2$(0), consisting of the $TiO_2$ rutile phase, as determined by the XRD measurements, contains nanocrystals with an elongated shape and can be found in large bundles. The thickness of the rods varies in the interval of 10–15 nm. However, large nanocrystals not formed from individual nanorods can be found. Sample $TiO_2$(0.3) with a $TiO_2$ rutile phase consists of highly elongated nanocrystals with a cylinder width of ≈10 nm. They are organized in bundles resembling a fan, consisting of many nanowires almost parallel. The sample $TiO_2$(0.5) has two noticeable phases: rutile and brookite. Rutile phase nanocrystals seem elongated and composed of closely packed, bundle-like structures. The bundles seem to have a conical shape and consist of many nanowires that are almost parallel to one another. The short dimension of the rutile nanocrystals is much smaller than their length. On the other hand, the nanocrystals belonging to the brookite phase are larger in width, shorter in length, and better dispersed, which was also confirmed by SAED measurements and by high-resolution images using the Fourier transform. Simulations of the diffraction patterns were made with Recipro software to ensure that the FFT measurements on the high-resolution images correctly describe the orientation and structure of the nanocrystals. The simulated images agree with the FFT patterns and are presented in Figures S1–S7 and S13–S16. Sample $TiO_2$(1.5) with mostly $TiO_2$ in an anatase phase shows small nanoparticles with a size of ∼7 nm that are dispersed but also form weakly bound clusters (see the distribution of the nanoparticle size in Figure S12). The nanoparticles seem to have slightly irregular shapes, with most elongating. Sample $TiO_2$(1.8) having a majority $TiO_2$-anatase phase resembles sample $TiO_2$(1.5), but the nanoparticles seem to be a little larger (≈7.4 nm) with a slightly wider size distribution.

Nitrogen adsorption–desorption isotherms (see Figure S8) were used with the BET method to determine the specific surface area of the $TiO_2$-based materials, presented in Table 1. The $TiO_2$ samples show a specific surface area in the 13–186 $m^2$ $g^{-1}$ range, where the increase in surface area is related to the anatase and brookite phases, which have smaller crystals. It is important to mention that anatase samples had specific surface areas higher than those of Degussa P25 $TiO_2$. Considering that only the illuminated surface participates in photocatalysis, it is essential to determine the BET surface area, the average pore diameter, and the shape of the pores. The adsorption isotherm analysis determined that all samples


https://doi.org/10.1021/acsomega.3c05890
ACS Omega 2023, 8, 41664–41673

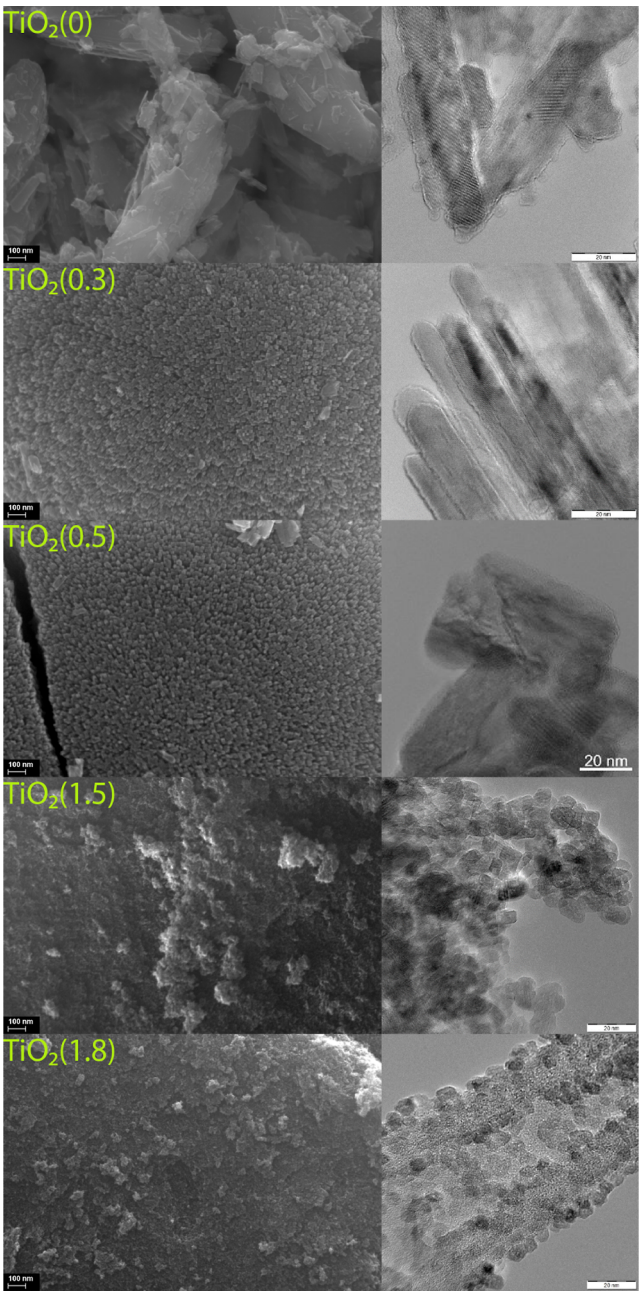


**Figure 3.** SEM (scale 100 nm) and TEM (scale 20 nm) images of the $TiO_2$ samples.

are mesoporous except for the nonporous $TiO_2(0)$ sample. The average pore diameter was calculated using the Barrett–Joyner–Halenda (BJH) model and is depicted in Figure S11. The pore size distribution curves show a sharp peak for samples $TiO_2(0.3)$, (0.5), (1.5), and (1.8), which correspond to the main pore diameters of 3.5, 4.3, 5.5, and 4 nm, respectively. Xiong et al.[57] also used hydrothermal methods for obtaining mesoporous $TiO_2$ with pore sizes of about 4.5–5.5 and 9–10.2 nm, which agreed with the ones presented in this study. On the other hand, by the sol–gel method, Szołdra et al.[58] obtained $TiO_2$ powder samples with pore sizes within the 2–100 nm range. $TiO_2(0.3)$, $TiO_2(0.5)$, and $TiO_2(P25)$ samples are characterized by type H3 hysteresis loops that suggest the existence of slit-like pores. The shape of the isotherms for $TiO_2(1.5)$ and $TiO_2(1.8)$ samples with type H2 hysteresis indicates the presence of ink bottle-shaped pores in the porous network, in which evaporation is delayed, desorption occurring through the neck section, while the wide pores remain filled until low values of relative pressure.[59,60]

The samples' band gap was determined using the Tauc plot (see Figure S10).[61] The band gap values from the absorption peaks were obtained by extrapolating the linear portion of the $(E \cdot \hbar \cdot \vartheta)^2$ curves versus photon energy to zero, summarized in Table 1. The samples $TiO_2(0)$, $TiO_2(0.3)$, and $TiO_2(0.5)$ had the lowest band gap values of 2.2, 2.4, and 2.9 eV, respectively. Samples $TiO_2(1.5)$ and $TiO_2(1.8)$ containing anatase as a majority phase had lower band gap values than that of Degussa P25 $TiO_2$ (3.3 eV), namely, 3.1 and 3.2 eV, respectively. All samples showed high absorption of visible light (from 380 to 430 nm), which means they can be activated with solar light.

X-Band EPR spectroscopy (9.88 GHz) was used to investigate the defect centers present in the $TiO_2$ samples investigated in this study. The results are presented in Figure 4,

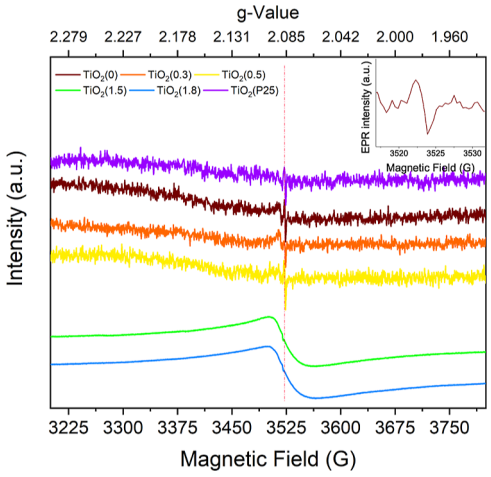


**Figure 4.** EPR spectra of the $TiO_2$-based samples.

where the $TiO_2$ samples exhibit a weak signal with a $g$-value $g_F$ = 2.0036 that we attributed, based on the literature, to a so-called F-center, an electron trapped in an oxygen vacancy,[62,63] which can be found in the EPR spectra of all samples with varying pH values, showing that this defect is not affected by the synthesis procedure employed to obtain the $TiO_2$-based materials. As observed in the XRD measurements, samples (0), (0.3), and (0.5) have a predominant rutile phase, while samples (1.5) and (1.8) have a minority (<20%) rutile phase. Thus, the EPR signal with $g$ = 2.0036 is related to this $TiO_2$ phase.

Samples (1.5) and (1.8), which have a majority anatase phase, exhibit an intense EPR signal with a large peak-to-peak line width (≈5.3 mT), which probably originates from oxygen-related defects (hole center) as already described in the literature.[64] The large line width indicates a high concentration of defect centers in the anatase-based $TiO_2$ samples, resulting in a strong exchange interaction between the paramagnetic centers. According to Zhou et al.,[5] defects are usually considered active sites in semiconductor photocatalysis, serving as recombination centers for electrons and holes. The oxygen vacancy defects in the bulk usually extend the photoresponse to the visible light region and improve the


https://doi.org/10.1021/acsomega.3c05890
ACS Omega 2023, 8, 41664–41673

separation of photogenerated electron−hole pairs. The effect of too few oxygen vacancy defects is limited due to the fewer active sites. However, once the amount of oxygen vacancy defects increases, they become photogenerated electron−hole recombination centers due to the great distortion of the crystal structure. The distorted crystal structure inhibits the rapid migration of photogenerated charge carriers to the surface for the subsequent photocatalytic reaction.

The efficiency of reactive oxygen species (ROS) photogeneration by TiO2-based samples was assessed by EPR using the spin-trapping agent 5,5-dimethyl-1-pyrroline-*N*-oxide (DMPO). DMPO can trap oxygen radicals produced during the photoexcitation of $TiO_2$,[65] collectively denoted by $^{\bullet}R$, forming more stable adducts DMPO + $^{\bullet}R \rightarrow {}^{\bullet}$DMPO−R. The nature of the trapped radicals can be identified by analyzing the hyperfine coupling constants in the experimental EPR spectra. The mechanisms for the primary events occurring at the catalyst surface have been described in the literature.[66] The first step in photocatalysis reactions is generating the hole−electron pairs by irradiating the $TiO_2$ particles with photonic energy equal to or greater than its band gap energy (3.2 eV). The electron is then extracted from the valence band (VB) to the conduction band (CB). This process produces a positive VB (hole $h^+$) region and a free electron ($e^-$) in the CB. The hole at the catalyst surface reacts with hydroxyl ions ($OH^-$) and adsorbs water to form free $OH^{-\bullet}$ radicals. The CB electron reduces oxygen to the superoxide ion, $O_2^{-\bullet}$. This reaction prevents $e^-/h^+$ recombination without other electron acceptors.

Figure S-19a−f† shows the set of EPR spectra monitored during the exposure of $TiO_2$ in mixed solvent water/DMSO (9:1 v/v). All samples excluding $TiO_2$(0.3) show ROS generation, while $TiO_2$(1.5) has the highest EPR signal and, therefore, the highest concentration of photogenerated ROS. The EPR spectra are complex, representing a superposition of the dominant six-line signal attributed to $^{\bullet}$DMPO−$CH_3$ and the low-intensity signal of $^{\bullet}$DMPO−OH (denoted by *) with slightly modified hyperfine coupling constants caused by the DMSO presence in the system.[67] The hyperfine constants determined from the spectrum were $a_N$ = 16.5 G and $a_H$ = 24 G for the $^{\bullet}$DMPO−$CH_3$ radical and $a_N = a_H$ = 14.8 G for the $^{\bullet}$DMPO−OH radical, which are in good agreement with values reported in the existing literature.[68]

**2.2. Degradation of RhB.** The photocatalytic property of $TiO_2$ depends on many parameters such as particle size, surface area, phase state, and band gap.[69−71] To activate the photocatalysts by generating pairs of charge carriers (electron $e^-$−hole $h^+$), ultraviolet light with a wavelength below 390 nm can induce electronic transitions in semiconductors. Based on this, the first experiment was performed with exposure to UV light with a 365 nm wavelength. At this wavelength, the dye remained stable and did not degrade independently. The second experiment was conducted under exposure to a sunlight simulator with an extensive spectral range of 250−2000 nm and 1 sun power, reproducing the sun's direct radiation spectrum on the ground at a 48.2 zenith angle.

Figure 5 shows the RhB degradation diagram, and Figure 6 shows the photocatalytic activity using a pseudo-first-order kinetic fit equation. The rhodamine B degradation rate constants, *k*, of the $TiO_2$ samples, are determined using eq 3 and are given in Table 2.

$$\ln(C_0/C) = k\cdot\tau \quad (3)$$

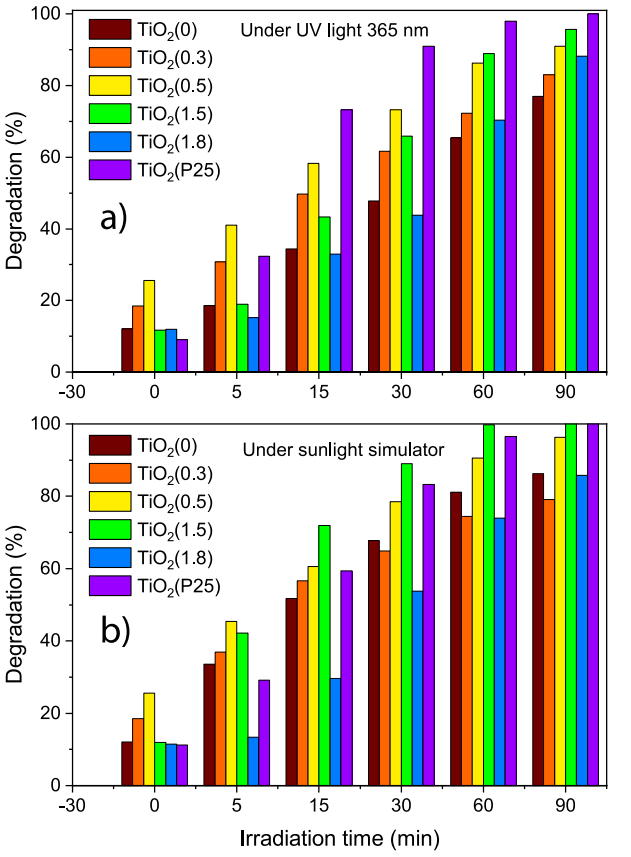


**Figure 5.** Decolorization diagram for rhodamine B degradation with $TiO_2$ nanoparticles under UV (365 nm) (a) and solar irradiation (b).

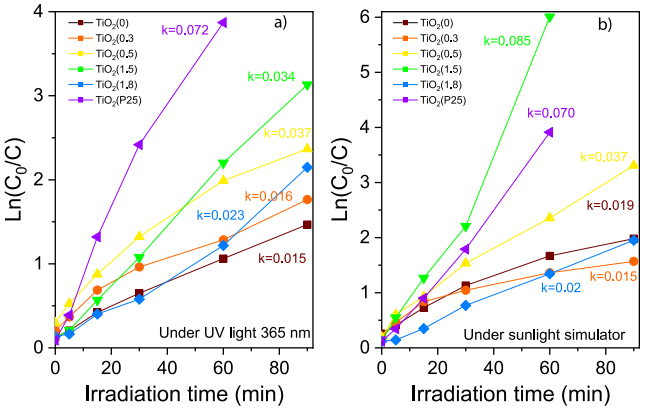


**Figure 6.** Kinetic plot for rhodamine B degradation with $TiO_2$ nanoparticles under UV (365 nm) (a) and solar (b) irradiation.

where $C_0$—initial concentration of rhodamine B; *C*—concentration after photocatalysis; *k*—rate constant of the reaction; $\tau$—irradiation time.

Comparing the degradation activity of the samples (see Table 2) under UV light, the best results show that the commercial P25 sample has a rate constant of 0.07 $min^{-1}$, and after 60 min irradiation, RhB was degraded to 98%. However, when the solar simulator was used, the $TiO_2$(1.5) sample, with 67% anatase, showed better results. The rate constant of the reaction is 0.08 $min^{-1}$ compared to 0.06 $min^{-1}$ for P25. Even though the anatase phase is not the main factor affecting the photoactivity, it significantly improves the ability of the photocatalyst to degrade the dye. Nevertheless, the sample


https://doi.org/10.1021/acsomega.3c05890
ACS Omega 2023, 8, 41664−41673

Table 2. Degradation Efficiency ($D_{365}$—under 365 nm and $D_{sol}$—under the Solar Light Simulator) and Reaction Rate ($k$) of the Studied Samples and Some Comparative Materials Used for the Degradation of RhB

| $TiO_2$ sample | $k_{365\ nm}$, $min^{-1}$ | $k_{solar}$ $min^{-1}$ | $t$ min | $D_{365}$% | $D_{sol}$ % | ref |
|---|---|---|---|---|---|---|
| (0) | 0.015 | 0.019 | 90 | 77 | 86 | this work |
| (0.3) | 0.016 | 0.015 | 90 | 83 | 79 | this work |
| (0.5) | 0.037 | 0.037 | 90 | 91 | 96 | this work |
| (1.5) | 0.034 | 0.085 | 90/60 | 95 | 99 | this work |
| (1.8) | 0.023 | 0.020 | 90 | 88 | 86 | this work |
| (P25) | 0.068 | 0.072 | 60 | 97 | 98 | this work |
| $MoS_2$/Ti | | 0.009 | 120 | | 100 | Zhou et al[72] |
| ZnO/FTO | 0.215 | | 30 | 99.98 | | Ait hssi et al[73] |
| Ce−$TiO_2$ | | | 480 | | 99.89 | Kasinathan et al[74] |
| N−$TiO_2$/FTO | 0.215 | | 30 | 64 | | Kothavale et al[75] |
| Mn−N/$TiO_2$/Ti | | 0.023 | 60 | | 74.2 | Nurdin et al[76] |
| Au/ZnO | | | 180 | | 95 | Ahmad et al[77] |
| $Fe_3O_4$ | | | 60 | | 97.6 | Wang et al[78] |
| $GeO_2$/$TiO_2$ | | | 180 | | 100 | Natarajan et al[79] |
| 48% rutile/52% anatase | | 0.1225 | 24 | | 94 | Singh et al[80] |

with a high rutile content, $TiO_2$(1.5), showed impressive results regardless of the irradiation source. The effect of the pH value on the photocatalysis process was investigated on a model solution of RhB with $TiO_2$(1.5). Even though the initial solution of RhB has a pH value of 7.07, adding the $TiO_2$(1.5) photocatalyst changes the pH to 3.8. Changing the pH value to 7 and 10 leads to a decrease in photocatalytic efficiency, as presented in Figure S17. According to Xue et al.,[81] $TiO_2$ shows a higher photocatalytic activity under acidic conditions due to the generation of active radicals such as $O_2^{\bullet-}$ and $OH^{\bullet}$ in the presence of oxygen in an aqueous medium.

The photostability of the photocatalyst was tested using the best-performing sample under UV irradiation, $TiO_2$(1.5), while six RhB degradation cycles were performed. The photocatalytic activity of the $TiO_2$(1.5) slowly reduced with each cycle without regeneration, but despite this, it remained high enough (see Figure S18).

The photocatalytic mechanism of the materials based on different $TiO_2$ phases can be described with the help of a so-called Z-scheme, where the band gap of the material is reduced while the CB potential is lowered, and the VB potential is lifted.[82,83] The Z-scheme photocatalysts are named as such because their charge transfer mechanism is similar to natural photosynthesis in green plants, in which the charge-carrier transport pathway involves a two-step photoexcitation that resembles the English letter "Z".[84]

In a study presented by Xu et al.,[85] the enhanced photocatalytic water splitting ability of an anatase/rutile biphase system was related to a Z-scheme mechanism. The photocatalytic activity of $H_2$ production via water splitting was higher for the anatase/rutile containing $TiO_2$ than for pure anatase and pure rutile because the mixed-phase $TiO_2$ materials act as a direct Z-scheme anatase/rutile photocatalyst, which greatly reduces the electron−hole recombination rate. In addition, the sample's electron−hole separation efficiency and redox ability are better than those of the single-phase $TiO_2$ materials because of the Z-scheme photocatalysts' high reduction and oxidation potentials.

Table 2 summarizes the degradation-related information on the proposed $TiO_2$ samples compared to other materials used to degrade the RhB dye. Materials like $MoS_2$/Ti reported by Zhou et al.[72] or Ce−$TiO_2$ reported by Kasinathan et al.[74] have very good degradation efficiency under solar light ≈100%, but the degradation process takes much longer (even up to 8 h) compared to the $TiO_2$(1.5) sample which achieves a degradation efficiency of 99% in only 1 h. It is also worth mentioning that in the presented case, no electrical potential was used to enhance the photocatalytic properties, as is the case for $Fe_3O_4$ reported by Wang et al.,[78] which had a degradation efficiency of 97.6% after 1 h. At the same time in this study, no dopant material was employed to influence the defect structure of the host $TiO_2$ material, which is the case for Mn and N codoped $TiO_2$/Ti reported by Nurdin et al.,[76] a feature controlled only by varying the pH value of the precursor solution. The high degradation efficiency (99%) of RhB under solar simulator light after only 1 h and the facile synthesis method make the proposed material an excellent candidate for further applications in the field of decontamination. Singh et al.[80] synthesized an anatase/rutile mixed $TiO_2$ phase with ball-like submicron structures and compared it to pure anatase. According to this study, the mixed $TiO_2$ sample has higher activity, while the sample with 48% rutile and 52% anatase phase of $TiO_2$ is found to be the most efficient photocatalyst leading to the degradation of 94% of 5 $\mu$M RhB in 24 min, whereas the sample containing pure anatase could degrade only 88% of 5 $\mu$M RhB under the same conditions. The degradation of RhB is found to obey first-order kinetics, and the rate constants are estimated to be 0.089 and 0.1225 $min^{-1}$ for the pure anatase sample and mixed-phase sample, respectively.

## 3. CONCLUSIONS

The $TiO_2$ nanoparticles were synthesized via a hydrothermal method using titanium tetrachloride as the precursor material. Using HCl for making acidic conditions during synthesis showed that the low pH value directly influenced the formation of the rutile $TiO_2$ phase and increasing the pH value leads to the formation of anatase and brookite phases. The analysis of the powders by XRD and Raman shows that the samples $TiO_2$(0) and $TiO_2$(0.3) consist of rutile with crystal sizes of 64 and 18 nm, respectively, and the nanopowder $TiO_2$(0.5) was determined as a mix of rutile/anatase/brookite with the ratio of the weight fraction 76:6:18 with a size of the rutile phase crystals of 14 nm. For $TiO_2$(1.5), the composition was determined as rutile/anatase/brookite 14:67:19 respectively, and for $TiO_2$(1.8) 12:64:24 (rutile/


https://doi.org/10.1021/acsomega.3c05890
ACS Omega 2023, 8, 41664−41673

anatase/brookite). The last two samples have a main anatase phase with a crystal size of anatase of 10 and 9 nm, respectively. The photocatalytic efficiency of the samples was tested by following the degradation of rhodamine B (RhB). All the presented samples show high photocatalytic activity under UV radiation, and due to their possibility to absorb visible light, they have a very good degradation efficiency under solar light irradiation. $TiO_2$(1.5) under solar irradiation shows the best RhB degradation constant rate, which is better than that of the reference P25, with a degradation efficiency of 99% after only 1 h of irradiation.

## 4. EXPERIMENTAL SECTION

**4.1. Material Synthesis.** Titanium tetrachloride ($TiCl_4$, Riedel-de Haen AG) was mixed with hydrochloric acid (HCl) with an initial concentration of 37% and diluted in deionized water. Before the mixture was transferred into a hydrothermal reactor, the mixture was stirred for 25 min. The solution was kept at 160 °C for 6 h, as presented in Scheme 1. The obtained

**Scheme 1. Synthesis Scheme of the $TiO_2$ Nanomaterials**

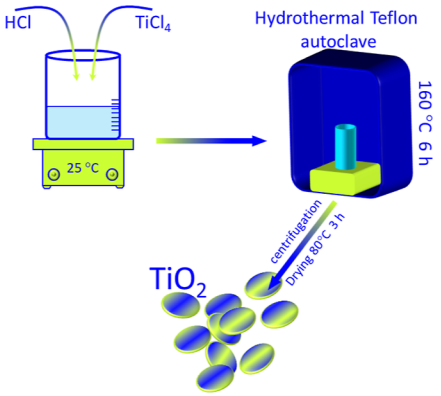


colloidal solution was washed and dried at 80 °C for 3 h, after which $TiO_2$ photocatalysts were obtained. No further thermal treatment process was performed. The nomenclature of the samples is given in the form $TiO_2$ (pH value).

**4.2. Characterization.** The crystal structure was characterized by an X-ray diffractometer D8 ADVANCE, Bruker, and a Raman spectrometer LabRAM HR Evolution, HORIBA, equipped with a 633 nm laser. The morphology was investigated using scanning electron microscopy (SEM) S0320-MVZ-5605, XEI Scientific Inc. The TEM studies were performed on an analytical electron microscope JEM-ARM 200F operated at 200 kV.

The textural analysis of the samples was performed through $N_2$ physisorption at −196 °C using a Micromeritics ASAP 2020 analyzer, Norcross, GA, USA. Before each measurement, the samples were degassed under a vacuum at 150 °C for 4 h. The specific surface areas were calculated by using the Brunauer−Emmett−Teller (BET) equation, and the total pore volume was estimated from the gas amount adsorbed at a relative pressure of 0.99 Pa. The pore size distribution (PSD) curves were obtained from the adsorption−desorption data using the Barrett−Joyner−Halenda (BJH) model. The paramagnetic defects and the photogeneration of ROS were characterized by electron paramagnetic resonance (EPR) spectroscopy in the X-band. For the measurements, an Elexsys 500 spectrometer equipped with an X-SHQ 4119HS-W1 Bruker resonator was used at a frequency of 9.88 GHz. The kinetics of the photogenerated ROS was determined by recording the EPR spectra of the $TiO_2$ suspensions in water in the presence of the 5,5-dimethyl-1-pyrroline-N-oxide (DMPO) spin trap, during continuous UV radiation (365 nm) exposure for 30 min. For UV irradiation, an M365FP1 UV diode from Thorlabs was used.

**4.3. Photocatalytic Experiment.** The $TiO_2$ photocatalyst (0.01 g) was mixed with rhodamine B dye ($C = 10^{-5}$ mol/L) in a glass chemical beaker. A sunlight simulator SF-300-A, Sciencetech, Canada, with a power of 1 sun and a UV lamp with wavelength 365 nm and power 36 W were employed to irradiate the solutions for different time intervals (5, 15, 30, 60, and 90 min), at the end of which a sample of the solution was taken to determine its concentration using the spectrophotometric method. The region between 30 and 0 min represents the concentration of RhB with the photocatalysts in the dark, where the equilibrium of the dye molecules was achieved, and denotes the dye adsorption stage of the photocatalysts. More adsorption on the catalyst reaction site leads to enhanced degradation of RhB. The amount of RhB adsorbed at its equilibrium concentration without UV light for 30 min and the degradation efficiency during photocatalysis were calculated with $\alpha = (C_0 - C_t)/C_0 \cdot 100\%$. Moreover, the equilibrium adsorption capacity was calculated as $q_e = [(C_0 - C_t) \cdot 1000 \cdot M_w \cdot V_0]/W_{cat}$[86] (the results are presented in Supporting Information Table T2†).

## ■ ASSOCIATED CONTENT

### Supporting Information

The Supporting Information is available free of charge at https://pubs.acs.org/doi/10.1021/acsomega.3c05890.

Low-magnification TEM, EDS figures, nitrogen adsorption−desorption isotherm graphs, Tauc's plot to determine the band gap energy value of the studied samples, PSD curves, high-magnification images, and EPR spectra (PDF)

## ■ AUTHOR INFORMATION


### Corresponding Authors

**Arpad Mihai Rostas** − *National Institute of Isotopic and Molecular Technologies, Cluj-Napoca 400293, Romania;* orcid.org/0000-0001-8190-9512; Email: arpad.rostas@itim-cj.ro

**Aurelian Catalin Galca** − *National Institute of Materials Physics, Magurele 077125, Romania;* orcid.org/0000-0002-1914-4210; Email: ac_galca@infim.ro

### Authors

**Anna Stepanova** − *National Institute of Materials Physics, Magurele 077125, Romania*

**Teddy Tite** − *National Institute of Materials Physics, Magurele 077125, Romania*

**Iryna Ivanenko** − *National Technical University of Ukraine Igor Sikorsky Kyiv Polytechnic Institute, Kyiv 03056, Ukraine*

**Monica Enculescu** − *National Institute of Materials Physics, Magurele 077125, Romania*

**Cristian Radu** − *National Institute of Materials Physics, Magurele 077125, Romania*

**Daniela Cristina Culita** − *Institute of Physical Chemistry Ilie Murgulescu, Romanian Academy, Bucharest 060021, Romania*

Complete contact information is available at:




https://doi.org/10.1021/acsomega.3c05890
ACS Omega 2023, 8, 41664−41673

https://pubs.acs.org/10.1021/acsomega.3c05890

### Author Contributions

A.S.: conceptualization, formal analysis, investigation, validation, results interpretation, writing—original draft, writing—review & editing; T.T.—conceptualization, methodology, validation, formal analysis, investigation, data curation, writing—review & editing; I.I.—conceptualization, methodology, validation, formal analysis, data curation; M.E.—investigation, formal analysis, resources; C.R.—formal analysis, investigation, results interpretation; D.C.C.—investigation; A.M.R.—conceptualization, investigation, formal analysis, visualization, validation, results interpretation, writing—original draft, writing—review and editing; A.C.G.—conceptualization, formal analysis, investigation, methodology, project administration, supervision, validation, writing—original draft, writing—review and editing.

### Notes

The authors declare no competing financial interest.

## ■ ACKNOWLEDGMENTS

The authors acknowledge funding by the Core Programs granted by the Romanian Ministry of Research, Innovation, and Digitization through the projects PN23080303, 35PFE/2022, and PN23240103.

## ■ REFERENCES

(1) Kyzas, G. Z.; Matis, K. A. Nanoadsorbents for pollutants removal: a review. *J. Mol. Liq.* **2015**, *203*, 159−168.
(2) Crini, G.; Lichtfouse, E.; Wilson, L. D.; Morin-Crini, N. Conventional and non-conventional adsorbents for wastewater treatment. *Environ. Chem. Lett.* **2019**, *17*, 195−213.
(3) Tegladza, I. D.; Xu, Q.; Xu, K.; Lv, G.; Lu, J. Electrocoagulation processes: a general review about role of electro-generated flocs in pollutant removal. *Process Saf. Environ. Prot.* **2021**, *146*, 169−189.
(4) Sadri Moghaddam, S.; Alavi Moghaddam, M.; Arami, M. Coagulation/flocculation process for dye removal using sludge from water treatment plant: optimization through response surface methodology. *J. Hazard Mater.* **2010**, *175*, 651−657.
(5) Zhou, M.; Chen, J.; Yu, S.; Chen, B.; Chen, C.; Shen, L.; Li, B.; Lin, H. The coupling of persulfate activation and membrane separation for the effective pollutant degradation and membrane fouling alleviation. *Chem. Eng. J.* **2023**, *451*, 139009.
(6) Joo, S. H.; Tansel, B. Novel technologies for reverse osmosis concentrate treatment: A review. *J. Environ. Manage.* **2015**, *150*, 322−335.
(7) Chiu, Y.-H.; Chang, T.-F. M.; Chen, C.-Y.; Sone, M.; Hsu, Y.-J. Mechanistic insights into photodegradation of organic dyes using heterostructure photocatalysts. *Catalysts* **2019**, *9*, 430.
(8) Kumar, S.; Sharma, R.; Sharma, R.; Gupta, A.; Dubey, K. K.; Khan, A.; Singhal, R.; Kumar, R.; Bharti, A.; Singh, P.; et al. $TiO_2$ based Photocatalysis membranes: An efficient strategy for pharmaceutical mineralization. *Sci. Total Environ.* **2022**, *845*, 157221.
(9) Linsebigler, A. L.; Lu, G.; Yates, J. T., Jr. Photocatalysis on $TiO_2$ surfaces: principles, mechanisms, and selected results. *Chem. Rev.* **1995**, *95*, 735−758.
(10) Wu, T.; Liu, G.; Zhao, J.; Hidaka, H.; Serpone, N. Photoassisted degradation of dye pollutants. V. Self-photosensitized oxidative transformation of rhodamine B under visible light irradiation in aqueous $TiO_2$ dispersions. *J. Phys. Chem. B* **1998**, *102*, 5845−5851.
(11) Fox, M. A.; Dulay, M. T. Heterogeneous photocatalysis. *Chem. Rev.* **1993**, *93*, 341−357.
(12) Hoffmann, M. R.; Martin, S. T.; Choi, W.; Bahnemann, D. W. Environmental applications of semiconductor photocatalysis. *Chem. Rev.* **1995**, *95*, 69−96.
(13) Fujihira, M.; Satoh, Y.; Osa, T. Heterogeneous photocatalytic oxidation of aromatic compounds on $TiO_2$. *Nature* **1981**, *293*, 206−208.
(14) Wang, D.; Sheng, T.; Chen, J.; Wang, H.-F.; Hu, P. Identifying the key obstacle in photocatalytic oxygen evolution on rutile $TiO_2$. *Nat. Catal.* **2018**, *1*, 291−299.
(15) Tuc Altaf, C.; Colak, T. O.; Rostas, A. M.; Popa, A.; Toloman, D.; Suciu, M.; Demirci Sankir, N.; Sankir, M. Impact on the Photocatalytic Dye Degradation of Morphology and Annealing-Induced Defects in Zinc Oxide Nanostructures. *ACS Omega* **2023**, *8*, 14952−14964.
(16) Teixeira, A. R. F. A.; Menezes de Oliveira, A. L.; Neatu, F.; Kuncser, A. C.; Galca, A. C.; Rostas, A. M.; dos Santos, I. M. G. Understanding the Photocatalytic Activity of Sodium Hexatitanate Nanoparticles for Pollutants Degradation: A Spectroscopic Insight. *ACS Appl. Nano Mater.* **2023**, *6*, 4477−4488.
(17) Daviðsdóttir, S.; Shabadi, R.; Galca, A. C.; Andersen, I. H.; Dirscherl, K.; Ambat, R. Investigation of DC magnetron-sputtered $TiO_2$ coatings: Effect of coating thickness, structure, and morphology on photocatalytic activity. *Appl. Surf. Sci.* **2014**, *313*, 677−686.
(18) Li, N.; Ma, J.; Zhang, Y.; Zhang, L.; Jiao, T. Recent developments in functional nanocomposite photocatalysts for wastewater treatment: a review. *Adv. Sustainable Syst.* **2022**, *6*, 2200106.
(19) Zhang, H.; Banfield, J. F. Structural characteristics and mechanical and thermodynamic properties of nanocrystalline $TiO_2$. *Chem. Rev.* **2014**, *114*, 9613−9644.
(20) Anucha, C. B.; Altin, I.; Bacaksiz, E.; Stathopoulos, V. N. Titanium Dioxide ($TiO_2$)-Based Photocatalyst Materials Activity Enhancement for Contaminants of Emerging Concern (CECs) Degradation: In the Light of Modification Strategies. *Chem. Eng. J. Adv.* **2022**, *10*, 100262.
(21) Goncearenco, E.; Morjan, I. P.; Fleaca, C. T.; Dumitrache, F.; Dutu, E.; Scarisoreanu, M.; Teodorescu, V. S.; Sandulescu, A.; Anastasescu, C.; Balint, I. Titania nanoparticles for photocatalytic degradation of ethanol under simulated solar light. *Beilstein J. Nanotechnol.* **2023**, *14*, 616−630.
(22) Zhang, J.; Li, M.; Feng, Z.; Chen, J.; Li, C. UV Raman spectroscopic study on $TiO_2$. I. Phase transformation at the surface and in the bulk. *J. Phys. Chem. B* **2006**, *110*, 927−935.
(23) Nakata, K.; Fujishima, A. $TiO_2$ photocatalysis: Design and applications. *J. Photochem. Photobiol., C* **2012**, *13*, 169−189.
(24) Panayotov, D. A.; Frenkel, A. I.; Morris, J. R. Catalysis and photocatalysis by nanoscale Au/$TiO_2$: perspectives for renewable energy. *ACS Energy Lett.* **2017**, *2*, 1223−1231.
(25) Wang, D.; Xiao, L.; Luo, Q.; Li, X.; An, J.; Duan, Y. Highly efficient visible light $TiO_2$ photocatalyst prepared by sol-gel method at temperatures lower than 300°C. *J. Hazard. Mater.* **2011**, *192*, 150−159.
(26) Zhu, J.; Ren, J.; Huo, Y.; Bian, Z.; Li, H. Nanocrystalline Fe/$TiO_2$ visible photocatalyst with a mesoporous structure prepared via a nonhydrolytic sol-gel route. *J. Phys. Chem. C* **2007**, *111*, 18965−18969.
(27) Liu, X.; Liu, Y.; Lu, S.; Guo, W.; Xi, B. Performance and mechanism into $TiO_2$/Zeolite composites for sulfadiazine adsorption and photodegradation. *Chem. Eng. J.* **2018**, *350*, 131−147.
(28) Tang, M.; Xia, Y.; Yang, D.; Liu, J.; Zhu, X.; Tang, R. Effects of hydrothermal time on structure and photocatalytic property of titanium dioxide for degradation of rhodamine b and tetracycline hydrochloride. *Materials* **2021**, *14*, 5674.
(29) Qi, W.; Du, J.; Peng, Y.; Wu, W.; Zhang, Z.; Li, X.; Li, K.; Zhang, K.; Gong, C.; Luo, M.; et al. Hydrothermal synthesis of $TiO_2$ nanorods arrays on ITO. *Mater. Chem. Phys.* **2018**, *207*, 435−441.
(30) Gupta, T.; Cho, J.; Cho, J.; Prakash, J. Hydrothermal synthesis of $TiO_2$ nanorods: formation chemistry, growth mechanism, and tailoring of surface properties for photocatalytic activities. *Mater. Today Chem.* **2021**, *20*, 100428.
(31) Rasheed, R. T.; Mansoor, H. S.; Qasim, B. H. Antibacterial activity of $TiO_2$ and $TiO_2$ composites nanopowders prepared by hydrothermal method. *Mater. Res. Express* **2019**, *6*, 0850a5.

(32) Khizir, H. A.; Abbas, T. A.-H. Hydrothermal growth and controllable synthesis of flower-shaped $TiO_2$ nanorods on FTO coated glass. *J. Sol-Gel Sci. Technol.* **2021**, *98*, 487−496.
(33) Bessergenev, V.; Khmelinskii, I.; Pereira, R.; Krisuk, V.; Turgambaeva, A.; Igumenov, I. Preparation of $TiO_2$ films by CVD method and its electrical, structural and optical properties. *Vacuum* **2002**, *64*, 275−279.
(34) Yu, J.-G.; Yu, H.-G.; Cheng, B.; Zhao, X.-J.; Yu, J. C.; Ho, W.-K. The effect of calcination temperature on the surface microstructure and photocatalytic activity of $TiO_2$ thin films prepared by liquid phase deposition. *J. Phys. Chem. B* **2003**, *107*, 13871−13879.
(35) Yuan, J.; Li, H.; Wang, Q.; Yu, Q.; Zhang, X.; Yu, H.; Xie, Y. Fabrication, characterization, and photocatalytic activity of double-layer $TiO_2$ nanosheet films. *Mater. Lett.* **2012**, *81*, 123−126.
(36) Chen, X.; Mao, S. S. Titanium dioxide nanomaterials: synthesis, properties, modifications, and applications. *Chem. Rev.* **2007**, *107*, 2891−2959.
(37) Baragau, I.-A.; Buckeridge, J.; Nguyen, K. G.; Heil, T.; Sajjad, M. T.; Thomson, S. A.; Rennie, A.; Morgan, D. J.; Power, N. P.; Nicolae, S. A.; et al. Outstanding visible light photocatalysis using nano-$TiO_2$ hybrids with nitrogen-doped carbon quantum dots and/or reduced graphene oxide. *J. Mater. Chem. A* **2023**, *11*, 9791−9806.
(38) Lavric, V.; Isopescu, R.; Maurino, V.; Pellegrino, F.; Pellutiè, L.; Ortel, E.; Hodoroaba, V.-D. A new model for nano-$TiO_2$ crystal birth and growth in hydrothermal treatment using an oriented attachment approach. *Cryst. Growth Des.* **2017**, *17*, 5640−5651.
(39) Dontsova, T.; Kyrii, S.; Yanushevska, O.; Suprunchuk, V.; Kosogina, I. Physicochemical properties of $TIO_2$, $ZrO_2$, $Fe_3O_4$ nanocrystalline adsorbents and photocatalysts. *Chem. Pap.* **2022**, *76*, 7667−7683.
(40) Popescu, T.; Oktaviani Matei, C.; Culita, D. C.; Maraloiu, V.-A.; Rostas, A. M.; Diamandescu, L.; Iacob, N.; Savopol, T.; Ilas, M. C.; Feder, M.; et al. Facile synthesis of low toxicity iron oxide/$TiO_2$ nanocomposites with hyperthermic and photo-oxidation properties. *Sci. Rep.* **2022**, *12*, 6887.
(41) Žerjav, G.; Žižek, K.; Zavašnik, J.; Pintar, A. Brookite vs. rutile vs. anatase: What's behind their various photocatalytic activities? *J. Environ. Chem. Eng.* **2022**, *10*, 107722.
(42) Luttrell, T.; Halpegamage, S.; Tao, J.; Kramer, A.; Sutter, E.; Batzill, M. Why is anatase a better photocatalyst than rutile?-Model studies on epitaxial $TiO_2$ films. *Sci. Rep.* **2014**, *4*, 4043.
(43) Li, H.; Shen, X.; Liu, Y.; Wang, L.; Lei, J.; Zhang, J. Facile phase control for hydrothermal synthesis of anatase-rutile $TiO_2$ with enhanced photocatalytic activity. *J. Alloys Compd.* **2015**, *646*, 380−386.
(44) Li, H.; Sun, B.; Gao, T.; Li, H.; Ren, Y.; Zhou, G. $Ti_3C_2$ MXene co-catalyst assembled with mesoporous $TiO_2$ for boosting photocatalytic activity of methyl orange degradation and hydrogen production. *Chin. J. Catal.* **2022**, *43*, 461−471.
(45) Zhu, Y.; Zhuang, Y.; Wang, L.; Tang, H.; Meng, X.; She, X. Constructing 0D/1D $Ag_3PO_4$/$TiO_2$ S-scheme heterojunction for efficient photodegradation and oxygen evolution. *Chin. J. Catal.* **2022**, *43*, 2558−2568.
(46) Li, J.; Wu, X.; Liu, S. Fluorinated $TiO_2$ hollow photocatalysts for photocatalytic applications. *Acta Phys.-Chim. Sin.* **2020**, *37*, 2009038.
(47) Zhao, B.; Lin, L.; He, D. Phase and morphological transitions of titania/titanate nanostructures from an acid to an alkali hydrothermal environment. *J. Mater. Chem. A* **2013**, *1*, 1659−1668.
(48) Reyes-Coronado, D.; Rodríguez-Gattorno, G.; Espinosa-Pesqueira, M.; Cab, C.; De Coss, R. d.; Oskam, G. Phase-pure $TiO_2$ nanoparticles: anatase, brookite and rutile. *Nanotechnology* **2008**, *19*, 145605.
(49) Campos, R. D.; Menezes de Oliveira, A. L.; Rostas, A. M.; Kuncser, A. C.; Negrila, C. C.; Galca, A.-C.; Félix, C.; Castellano, L.; da Silva, F. F.; dos Santos, I. M. G. $TiO_2$/ZIF-67 nanocomposites synthesized by the microwave-assisted solvothermal method: a correlation between the synthesis conditions and antimicrobial properties. *New J. Chem.* **2023**, *47*, 2177−2188.
(50) Kibasomba, P. M.; Dhlamini, S.; Maaza, M.; Liu, C.-P.; Rashad, M. M.; Rayan, D. A.; Mwakikunga, B. W. Strain and grain size of $TiO_2$ nanoparticles from TEM, Raman spectroscopy and XRD: The revisiting of the Williamson-Hall plot method. *Results Phys.* **2018**, *9*, 628−635.
(51) Ross, J. R.. In *Contemporary Catalysis*; Ross, J. R., Ed.; Elsevier: Amsterdam, 2019, pp 121−132.
(52) Holzwarth, U.; Gibson, N. The Scherrer equation versus the'Debye-Scherrer equation. *Nat. Nanotechnol.* **2011**, *6*, 534−535.
(53) Bouzid, S. A.; Galca, A. C.; Sajieddine, M.; Kuncser, V.; Rostas, A. M.; Iacob, N.; Enculescu, M.; Amarande, L.; Pasuk, I.; Essoumhi, A. Magneto-functionalities of $La_{1-x}A_xMnO_3$ (A= K; Ba) synthesized by flash combustion method. *J. Alloys Compd.* **2020**, *839*, 155546.
(54) El Khouja, O.; Galca, A. C.; Nouneh, K.; Zaki, M. Y.; Ebn Touhami, M.; Taibi, M.; Matei, E.; Negrila, C. C.; Enculescu, M.; Pintilie, L. Structural, morphological and optical properties of Cu−Fe−Sn−S thin films prepared by electrodeposition at fixed applied potential. *Thin Solid Films* **2021**, *721*, 138547.
(55) Hubbard, C. R.; Snyder, R. L. RIR-measurement and use in quantitative XRD. *Powder Diffr.* **1988**, *3*, 74−77.
(56) Iliev, M.; Hadjiev, V.; Litvinchuk, A. Raman and infrared spectra of brookite ($TiO_2$): experiment and theory. *Vib. Spectrosc.* **2013**, *64*, 148−152.
(57) Xiong, H.; Wu, L.; Liu, Y.; Gao, T.; Li, K.; Long, Y.; Zhang, R.; Zhang, L.; Qiao, Z.-A.; Huo, Q.; et al. Controllable synthesis of mesoporous $TiO_2$ polymorphs with tunable crystal structure for enhanced photocatalytic $H_2$ production. *Adv. Energy Mater.* **2019**, *9*, 1901634.
(58) Szołdra, P.; Frąc, M.; Pichór, W. Effect of sol composition on the properties of $TiO_2$ powders obtained by the sol-gel method. *Powder Technol.* **2021**, *387*, 261−269.
(59) Thommes, M.; Kaneko, K.; Neimark, A. V.; Olivier, J. P.; Rodriguez-Reinoso, F.; Rouquerol, J.; Sing, K. S. Physisorption of gases, with special reference to the evaluation of surface area and pore size distribution (IUPAC Technical Report). *Pure Appl. Chem.* **2015**, *87*, 1051−1069.
(60) Sing, K. S. Reporting physisorption data for gas/solid systems with special reference to the determination of surface area and porosity (Recommendations 1984). *Pure Appl. Chem.* **1985**, *57*, 603−619.
(61) Makuła, P.; Pacia, M.; Macyk, W. How to correctly determine the band gap energy of modified semiconductor photocatalysts based on UV−Vis spectra. *J. Phys. Chem. Lett.* **2018**, *9*, 6814−6817.
(62) Howe, R. F.; Gratzel, M. EPR observation of trapped electrons in colloidal titanium dioxide. *J. Phys. Chem.* **1985**, *89*, 4495−4499.
(63) Misra, S.; Andronenko, S.; Tipikin, D.; Freed, J.; Somani, V.; Prakash, O. Study of paramagnetic defect centers in as-grown and annealed $TiO_2$ anatase and rutile nanoparticles by a variable-temperature X-band and high-frequency (236 GHz) EPR. *J. Magn. Magn. Mater.* **2016**, *401*, 495−505.
(64) Kumar, C. P.; Gopal, N. O.; Wang, T. C.; Wong, M.-S.; Ke, S. C. EPR investigation of $TiO_2$ nanoparticles with temperature-dependent properties. *J. Phys. Chem. B* **2006**, *110*, 5223−5229.
(65) Benabbou, A.; Derriche, Z.; Felix, C.; Lejeune, P.; Guillard, C. Photocatalytic inactivation of Escherischia coli: Effect of concentration of $TiO_2$ and microorganism, nature, and intensity of UV irradiation. *Appl. Catal., B* **2007**, *76*, 257−263.
(66) Ollis, D. F. Contaminant degradation in water. *Environ. Sci. Technol.* **1985**, *19*, 480−484.
(67) Zalibera, M.; Rapta, P.; Staško, A.; Brindzová, L.; Brezová, V. Thermal generation of stable spin trap adducts with super-hyperfine structure in their EPR spectra: An alternative EPR spin trapping assay for radical scavenging capacity determination in dimethylsulphoxide. *Free Radic. Res.* **2009**, *43*, 457−469.
(68) Dvoranová, D.; Barbieriková, Z.; Brezová, V. Radical intermediates in photoinduced reactions on $TiO_2$ (an EPR spin trapping study). *Molecules* **2014**, *19*, 17279−17304.


https://doi.org/10.1021/acsomega.3c05890
*ACS Omega* 2023, 8, 41664−41673

(69) Rajeshwar, K.; Thomas, A.; Janáky, C. Photocatalytic activity of inorganic semiconductor surfaces: myths, hype, and reality. *J. Phys. Chem. Lett.* **2015**, *6*, 139−147.
(70) Xu, N.; Shi, Z.; Fan, Y.; Dong, J.; Shi, J.; Hu, M. Z.-C. Effects of particle size of $TiO_2$ on photocatalytic degradation of methylene blue in aqueous suspensions. *Ind. Eng. Chem. Res.* **1999**, *38*, 373−379.
(71) Brancho, J. J.; Bartlett, B. M. Challenges in co-alloyed titanium oxynitrides, a promising class of photochemically active materials. *Chem. Mater.* **2015**, *27*, 7207−7217.
(72) Zhou, Y.; Fan, X.; Zhang, G.; Dong, W. Fabricating MoS2 nanoflakes photoanode with unprecedented high photoelectrochemical performance and multi-pollutants degradation test for water treatment. *Chem. Eng. J.* **2019**, *356*, 1003−1013.
(73) Ait hssi, A.; Amaterz, E.; Labchir, N.; Atourki, L.; Bouderbala, I. Y.; Elfanaoui, A.; Benlhachemi, A.; Ihlal, A.; Bouabid, K. Electrodeposited ZnO nanorods as efficient photoanodes for the degradation of rhodamine B. *Phys. Status Solidi A* **2020**, *217*, 2000349.
(74) Kasinathan, K.; Kennedy, J.; Elayaperumal, M.; Henini, M.; Malik, M. Photodegradation of organic pollutants RhB dye using UV simulated sunlight on ceria based $TiO_2$ nanomaterials for antibacterial applications. *Sci. Rep.* **2016**, *6*, 38064.
(75) Kothavale, V.; Kanamadi, C.; Patil, P. Synthesis and characterization of sprayed nitrogen doped $TiO_2$ Thin films. *Mater. Today: Proc.* **2021**, *43*, 2721−2724.
(76) Nurdin, M.; Wibowo, D.; Azis, T.; Safitri, R. A.; Maulidiyah, M.; Mahmud, A.; Mustapa, F.; Ruslan, R.; Agus Salim, L. O.; Arham, Z.; et al. Photoelectrocatalysis Response with Synthetic Mn−N−$TiO_2$/Ti Electrode for Removal of Rhodamine B Dye. *Surf. Eng. Appl. Electrochem.* **2022**, *58*, 125−134.
(77) Ahmad, M.; Rehman, W.; Khan, M. M.; Qureshi, M. T.; Gul, A.; Haq, S.; Ullah, R.; Rab, A.; Menaa, F. Phytogenic fabrication of ZnO and gold decorated ZnO nanoparticles for photocatalytic degradation of Rhodamine B. *J. Environ. Chem. Eng.* **2021**, *9*, 104725.
(78) Wang, Q.; Jin, R.; Yin, C.; Wang, M.; Wang, J.; Gao, S. Photoelectrocatalytic removal of dye and Cr (VI) pollutants with $Ag_2S$ and $Bi_2S_3$ co-sensitized $TiO_2$ nanotube arrays under solar irradiation. *Sep. Purif. Technol.* **2017**, *172*, 303−309.
(79) Natarajan, K.; Bajaj, H. C.; Tayade, R. J. Effective removal of organic pollutants using $GeO_2$/$TiO_2$ nanoparticle composites under direct sunlight. *Mater. Chem. Front.* **2018**, *2*, 741−751.
(80) Singh, J.; Sahu, K.; Satpati, B.; Mohapatra, S. Facile synthesis, structural, optical and photocatalytic properties of anatase/rutile mixed phase $TiO_2$ ball-like sub-micron structures. *Optik* **2019**, *188*, 270−276.
(81) Xue, G.; Liu, H.; Chen, Q.; Hills, C.; Tyrer, M.; Innocent, F. Synergy between surface adsorption and photocatalysis during degradation of humic acid on $TiO_2$/activated carbon composites. *J. Hazard. Mater.* **2011**, *186*, 765−772.
(82) Qi, K.; Cheng, B.; Yu, J.; Ho, W. A review on $TiO_2$-based Z-scheme photocatalysts. *Chin. J. Catal.* **2017**, *38*, 1936−1955.
(83) Sato, S.; Arai, T.; Morikawa, T.; Uemura, K.; Suzuki, T. M.; Tanaka, H.; Kajino, T. Selective $CO_2$ conversion to formate conjugated with $H_2O$ oxidation utilizing semiconductor/complex hybrid photocatalysts. *J. Am. Chem. Soc.* **2011**, *133*, 15240−15243.
(84) Tachibana, Y.; Vayssieres, L.; Durrant, J. R. Artificial photosynthesis for solar water-splitting. *Nat. Photonics* **2012**, *6*, 511−518.
(85) Xu, F.; Xiao, W.; Cheng, B.; Yu, J. Direct Z-scheme anatase/rutile bi-phase nanocomposite $TiO_2$ nanofiber photocatalyst with enhanced photocatalytic $H_2$-production activity. *Int. J. Hydrogen Energy* **2014**, *39*, 15394−15402.
(86) Wang, R.; Shi, K.; Huang, D.; Zhang, J.; An, S. Synthesis and degradation kinetics of $TiO_2$/GO composites with highly efficient activity for adsorption and photocatalytic degradation of MB. *Sci. Rep.* **2019**, *9*, 18744.


https://doi.org/10.1021/acsomega.3c05890
*ACS Omega* 2023, 8, 41664−41673